Xiao-Ping Zhou,[1,2] Lang-Hua Li,[1] and Filippo Berto[3]

Cracking Behaviors of Rock-Like Specimens Containing Two Sets of Preexisting Cross Flaws under Uniaxial Compression

Reference

ABSTRACT

Cross flaws occur widely in rock masses and play a crucial role in the failure of rock engineering. This article first experimentally studies the cracking behaviors of rock-like specimens containing two sets of preexisting cross flaws under uniaxial compression. The effects of the flaw inclination angle and the horizontal spacing on the cracking behaviors of rock-like specimens are investigated as well as initiation stress, peak strength, peak strain, and complete stress–strain curves. The experimental results include observations of five types of cracks and seven types of coalescence. The crack initiation mode depends more strongly on the inclination angle than on the horizontal spacing. Moreover, it is found that a set of preexisting flaws coalesce not only with another set of preexisting flaws but also with the identical set of preexisting flaws. The peak strength and peak strain first increase and then decrease as the horizontal spacing increases. Meanwhile, the peak strength first increases and then decreases, and the peak strain first decreases, then increases, and finally decreases as the flaw inclination angle increases. This study provides a better understanding of the mechanical properties and fracture behaviors of rock masses, in particular those containing preexisting flaws that appear in sets or groups with similar orientation and characteristics.

[1] State Key Laboratory of Coal Mine Disaster Dynamics and Control, Chongqing University, No. 174 Shazhengjie, Shapingba, Chongqing 400044, China

[2] School of Civil Engineering, Chongqing University, No. 174 Shazhengjie, Shapingba, Chongqing 400044, China (Corresponding author), e-mail: xiao_ping_zhou@126.com, https://orcid.org/0000-0003-1551-6504

[3] Department of Mechanical Engineering, Norwegian University of Science and Technology, NTNU in Gjøvik, Postboks 191, NO-2802 Gjøvik, Trondheim 7491, Norway

Keywords

rock-like material, cross flaws, crack initiation, crack coalescence, crack initiation stress, mechanical behaviors

Introduction

A rock mass contains numerous cross joints and fissures that appear in sets or groups with similar orientation and characteristics [1–4]. These cross joints and fissures weaken the strength and stiffness of a rock mass. Moreover, they may potentially propagate and coalesce with each other, which results in further damage to the rock mass [2,4–6]. The degradation of mechanical properties induced by these primary discontinuities plays a crucial role in the failure of geotechnical structures, such as tunnels, rocky slopes, dams, and so on [7–10]. For example, as shown in **Fig. 1**, the failure of Delabole Slate Quarry slope was induced by the propagation of primary discontinuities [11], as were the Aishihik River Landslide and the

FIG. 1

Failure of Delabole Slate Quarry slope in 2012: (a) the planar failure in Delabole Quarry slope; (b) discontinuity mapping (the photograph is from Ref. [11]).

(a)
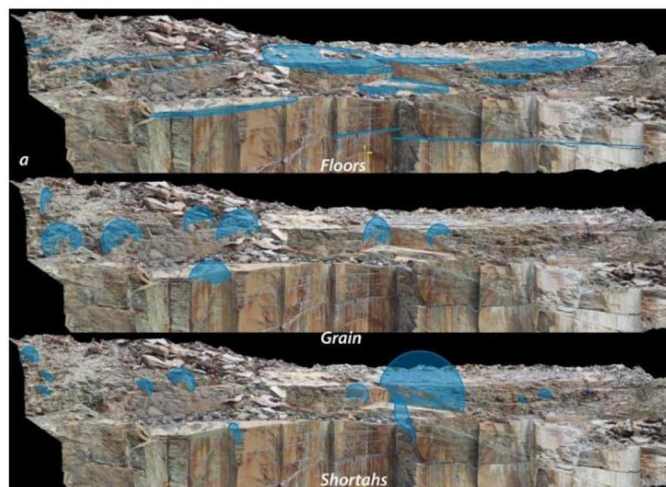
(b)

Randa Rockslide [12–15]. Therefore, it is necessary to study the mechanical properties and cracking behaviors of rock masses containing primary cross discontinuities.

Many experimental studies [1,2,5,6,10,16–25] have been performed to study the mechanical properties and cracking behaviors of rock or rock-like specimens containing preexisting flaws under uniaxial compressive loads. The previous works focused mainly on preexisting straight flaws. For rock or rock-like specimens containing a single preexisting flaw, the peak strength and elastic modulus weaken as expected to different extents because of the degradation effects induced by the preexisting flaw [1]. Moreover, two types of cracks, i.e., the wing crack and secondary crack, have been observed [1,3,17–19]. Wong and Zhang [3] further reported a third type of crack called the "mixed tensile-shear crack." For rock and rock-like specimens containing two preexisting straight flaws, both the mechanical properties and the cracking behaviors are different from those of specimens with a single preexisting straight flaw [5,7,23,26–33]. The main difference lies in the crack coalescence types induced by the interaction of two preexisting flaws. Three types of crack coalescence, i.e., tensile mode, shear mode, and mixed tensile-shear mode, were observed by Wong and Chau [7]. Moreover, the peak strength of specimens containing two preexisting flaws is obviously lower than the peak strength of specimens containing a single preexisting flaw [23,34]. The experimental observations are helpful to better understand the mechanical and cracking behaviors of rocks.

Uniaxial compressive tests on rock or rock-like specimens containing three or more preexisting straight flaws were performed to study the resulting mechanical and cracking behaviors [2,24,35–39]. These works mainly focused on the initiation, growth, and coalescence of cracks as well as the complete stress–strain curves of the flawed specimens. Some novel and complex behaviors associated with the mechanical properties and geometric morphometrics were observed in these studies. For example, out-of-plane tensile cracks and out-of-plane shear cracks were reported by Zhou, Cheng, and Feng [2]; the peak strength of flawed specimens does not depend on the density of preexisting flaws but on the actual number of preexisting flaws involved in the coalescence [35]. However, the previous works mainly focused on straight flaws. Note that a rock mass may contain numerous cross joints and fissures that occur in sets or groups with similar orientation and characteristics [1–4]. It can be reasonably inferred that the effects of multiple sets of cross flaws on the mechanical properties and the cracking behaviors are different from the effects of straight flaws. In this article, therefore, the initiation, growth, and coalescence of cracks in a rock-like specimen with two sets of preexisting cross flaws under uniaxial compression are investigated, along with their mechanical properties.

This article is organized as follows: Specimen preparation and testing system are presented in "Specimen Preparation Testing System." Experimental results, which include the obtained mechanical properties and cracking behaviors of rock-like specimens containing two sets of preexisting cross flaws, are presented and analyzed in "Analyses of Experimental Results." Conclusions are finally drawn in the last section.

Specimen Preparation and Testing System

SPECIMEN PREPARATION AND GEOMETRIC SETTING OF PREEXISTING FLAW

The mixture used as the modeling material consists of river sand, gypsum, cement, and water in a mass ratio of 12:1:1:2. The π factors in the dimensional analysis of this artificial material are comparable to the physical ranges of the π factors for Chongqing sandstone.

The dimensions of the rectangular specimens containing two sets of cross flaws are 150 mm high, 90 mm wide, and 70 mm thick. In this article, the term "flaw" is used to describe an artificially created crack or fracture; however, the term "crack" is adopted to describe a new fracture that nucleates and propagates under compressive loads [34,39]. Two sets of cross flaws are created by inserting steel shims into four slots in the mold template and removing them during curing. The thickness and width of the steel shim are, respectively, 2 mm and 20 mm. The materials are weighed using an electronic balance to ±0.01 kg. Three specimens with the same parameters are manufactured and tested in the same experiments to avoid accidental error. As shown in **Fig. 2**, flaw ① is perpendicular to flaw ②, which is parallel to flaw ④, and flaw ③ is perpendicular to flaw ④. The inclination angle α of preexisting flaws, as defined in **Fig. 2**, varies from 0° to 60° with an interval of 15°. The horizontal spacing S_h between the intersection points of preexisting flaws varies from 0 mm to 20 mm with an interval of 10 mm. The preexisting flaw length 2a is fixed to 20 mm, and the vertical spacing S_v between intersection points of preexisting flaws is fixed to 40 mm. A detailed description of the geometry of preexisting cross flaws is shown in **Table 1**.

IMAGE RECORDING SYSTEM AND TESTING PROCEDURE

Uniaxial compression tests of specimens are conducted using an AGI-250KN type precision electronic material testing machine, as shown in **Fig. 3**. Axial stress is imposed on the surface of rock-like specimens until failure occurs, and the failure is identified through a drop in the applied load. All tests are conducted under displacement-controlled conditions at an average loading rate of 1 mm/min. The load and the deformation of specimens are simultaneously recorded throughout the process of testing. Moreover,

FIG. 2

Specimen containing two sets of preexisting cross flaws under uniaxial compression: (a) front view on rock-like specimen; (b) vertical view on rock-like specimen; and (c) schematic diagram showing the geometry of cross flaws.
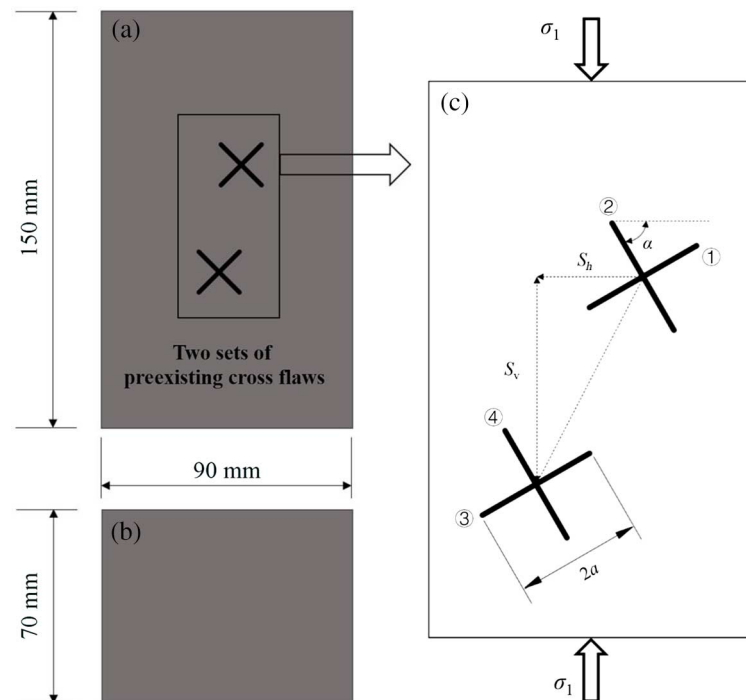
TABLE 1

Geometry parameters of preexisting cross flaws.

Specimen Number	Flaw Inclination Angle (α, °)	Flaw Length (2a, mm)	Horizontal Spacing (S_h, mm)	Vertical Spacing (S_v, mm)
A1	0	20	0	40
A2	0	20	10	40
A3	0	20	20	40
B1	30	20	0	40
B2	30	20	10	40
B3	30	20	20	40
C1	45	20	0	40
C2	45	20	10	40
C3	45	20	20	40
D1	60	20	0	40
D2	60	20	10	40
D3	60	20	20	40

the relationship between the real-time crack coalescence process and the axial stress–strain behavior of the rock-like material containing preexisting cross flaws is investigated using a photographic monitoring technique. The cracking behaviors of each specimen are monitored using an RDT/16 high-speed dynamic analysis system (DEL Imaging Systems LLC, Cheshire, CT), of which the frame rate can reach 100,000 frames per second, as shown in **Fig. 4**. The RDT/16 system can automatically collect data and capture high-resolution images when the cracking behaviors occur or specimen failure appears. In the present experiments, the capturing of images is completely synchronized with the loading.

FIG. 3

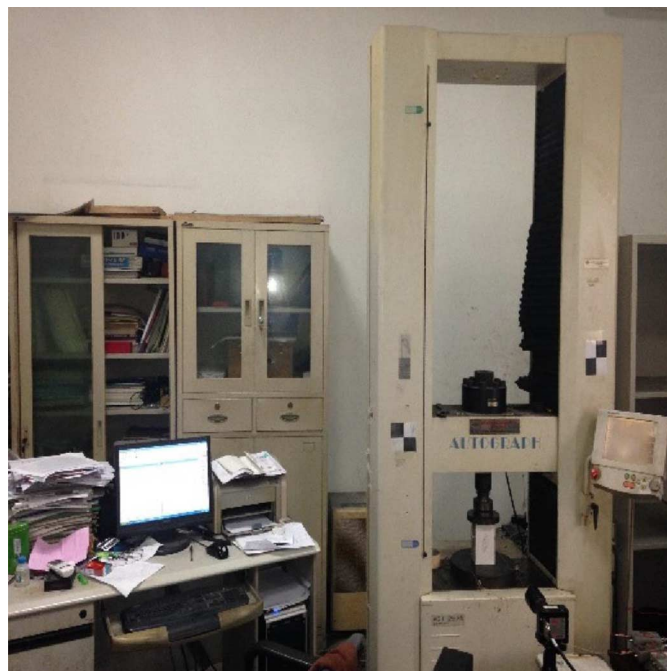AGI-250KN type precision electronic material testing machine.

FIG. 4

RDT/16 high-speed dynamic analysis system.

Analyses of Experimental Results

MECHANICAL PROPERTIES OF ROCK-LIKE SPECIMENS CONTAINING TWO CROSS FLAWS

As reported by Zhou, Cheng, and Feng [2], the mechanical properties of flawed specimens obviously differ from the mechanical properties of intact specimens because of the degradation induced by extensile microcracks. It is necessary to study the effects of preexisting flaws on the mechanical properties of flawed specimens. The complete axial stress–strain curves of specimens are discussed in depth, along with the initiation stress, the peak strength, and the peak strain. In this article, the flaw inclination angle α varies from 0° to 60°, and the horizontal spacing S_h varies from 0 mm to 20 mm.

The Complete Axial Stress–Strain Curves of Rock-Like Specimens with the Same Flaw Inclination Angle

Fig. 5a shows the complete axial stress–strain curves of specimens with a flaw inclination angle α of 0°. The complete axial stress–strain curves include four stages: the initial compaction stage, the elastic stage, the nonlinear hardening stage, and the strain-softening stage. Among these three specimens, the initial compaction for specimen A2

($S_h = 10$ mm) is the largest, while the initial compaction for specimen A1 ($S_h = 0$ mm) is the smallest. The peak strength for specimen A3 ($S_h = 20$ mm) is the lowest, while the peak strength for specimen A2 ($S_h = 10$ mm) is the highest. Quantitatively, the peak strengths for specimens A1, A2, and A3 are 1.931, 2.008, and 1.646 MPa, respectively. Moreover, the maximum peak strain of 0.824 % among the three specimens occurs in specimen A2 ($S_h = 10$ mm), whereas the minimum peak strain is 0.582 % (for specimen A1).

Fig. 5b shows the complete axial stress–strain curves of specimens with a flaw inclination angle α of 30°. The complete axial stress–strain curves likewise include four stages: the initial compaction stage, the elastic stage, the nonlinear hardening stage, and the strain-softening stage. Among these three specimens, the initial compaction for specimen B1 ($S_h = 0$ mm) is obviously smaller than for specimens B2 ($S_h = 10$ mm) and B3 ($S_h = 20$ mm), while the initial compaction for specimen B3 ($S_h = 20$ mm) is the greatest. The peak strength for specimen B3 ($S_h = 20$ mm) is lowest (2.121 MPa), while the peak strength for specimen B2 ($S_h = 10$ mm) is highest (2.466 MPa). The peak strain of the specimen with $S_h = 10$ mm is highest at 0.63 % (specimen B2), which is 0.1 % larger than for specimen B3, while the peak strain of the specimen with $S_h = 0$ mm is lowest.

FIG. 5 Axial stress–strain curves of specimens containing two sets of preexisting cross flaws with horizontal spacing of 0 mm, 10 mm, and 20 mm under uniaxial compressive loads: (a) flaw inclination angle $\alpha = 0°$; (b) flaw inclination angle $\alpha = 30°$; (c) flaw inclination angle $\alpha = 45°$; and (d) flaw inclination angle $\alpha = 60°$.
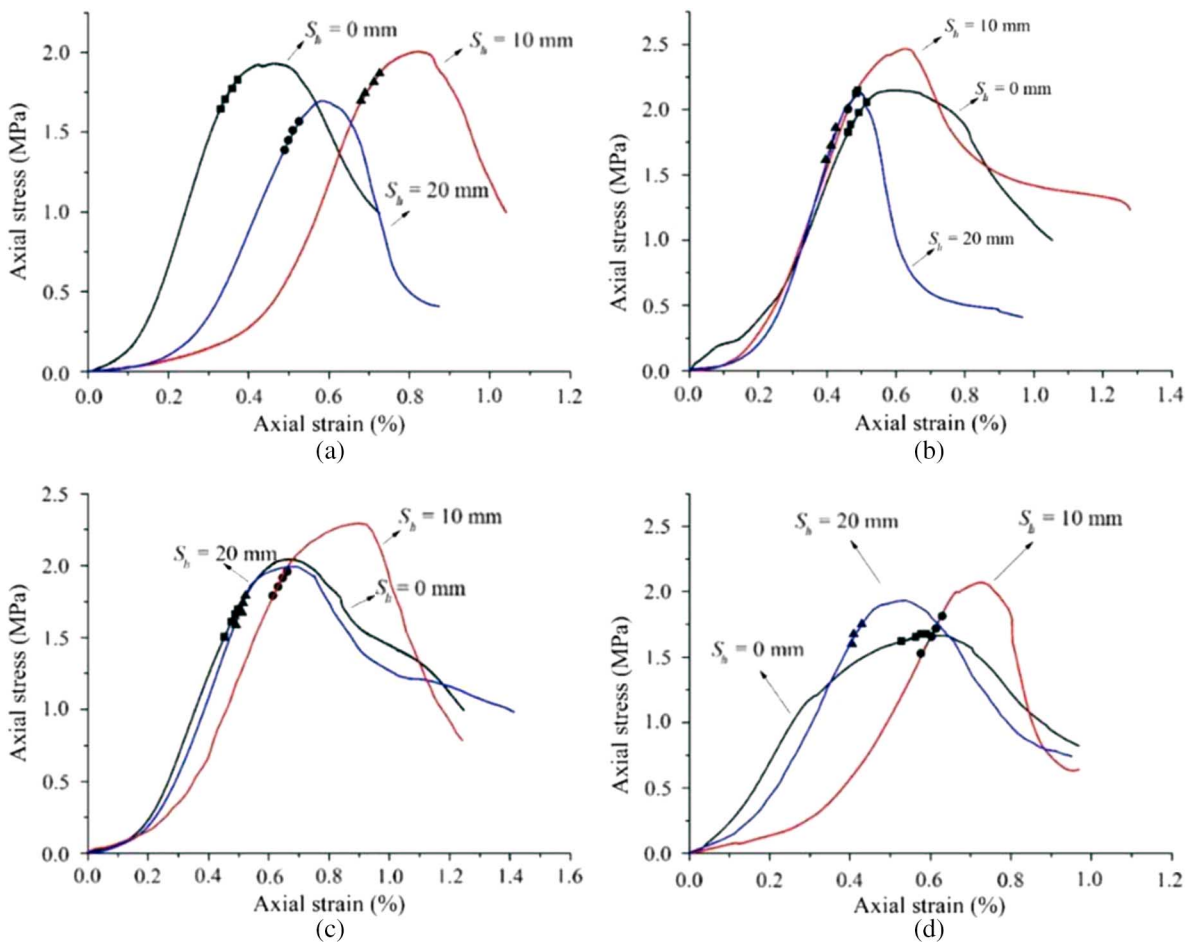
Fig. 5c shows the complete axial stress–strain curves of specimens with a flaw inclination angle α of 45°. The complete axial stress–strain curves can be summarized as four stages, i.e., the initial compaction stage, the elastic stage, the nonlinear hardening stage, and the strain-softening stage. The initial compaction for specimen C2 ($S_h = 10$ mm) is obviously greater than for specimens C1 ($S_h = 0$ mm) and C3 ($S_h = 20$ mm). Note that the initial compaction for specimen C1 ($S_h = 0$ mm) is the smallest. The peak strength for specimen C3 ($S_h = 20$ mm) is lowest (2.003 MPa), while the peak strength for specimen C2 ($S_h = 10$ mm) is highest (2.301 MPa). Moreover, the maximum peak strain among these three specimens occurs in specimen C2 ($S_h = 10$ mm) at 0.853 %, whereas the minimum peak strain is 0.653 % (for specimen C3).

Fig. 5d shows the complete axial stress–strain curves of specimens with a flaw inclination angle α of 60°. Clearly, the complete axial stress–strain curves include the initial compaction stage, the elastic stage, the nonlinear hardening stage, and the strain-softening stage. The initial compaction for specimen D2 ($S_h = 10$ mm) is obviously larger than for specimens D1 ($S_h = 0$ mm) and D3 ($S_h = 20$ mm). The peak strength for specimen D1 with $S_h = 0$ mm is the lowest (1.665 MPa), while the peak strength for specimen D2 ($S_h = 10$ mm) is the highest (2.074 MPa). Moreover, the maximum peak strain among the three specimens occurs in specimen D2 ($S_h = 10$ mm) at 0.722 %, whereas the minimum peak strain is 0.536 % (for specimen D3).

Effects of Horizontal Spacing on the Peak Strength of Rock-Like Specimens

The peak strength of specimens with different horizontal spacing is plotted in **Fig. 6** and shown in **Table 2**. **Fig. 6** shows that the peak strength of specimens first increases and then decreases as horizontal spacing S_h varies from 0 mm to 20 mm, and it reaches its maximum value when S_h equals 10 mm. For a flaw inclination angle α of 0°, the peak strength of the specimen with S_h of 10 mm reaches 2.008 MPa, which is, respectively, 0.077 MPa and 0.362 MPa larger than the peak strength of specimens with S_h of 0 mm and S_h of 20 mm. Moreover, for a flaw inclination angle α of 30°, the peak strength of the specimen with S_h of 10 mm equals 2.466 MPa. Compared with specimens B1 and B3, the peak strength of specimen B2 increases by 0.315 MPa and 0.345 MPa, respectively. For a flaw inclination angle α of 45°, the peak strength of the specimen with S_h of 0 mm is 2.046 MPa, and the value increases to 2.301 MPa when S_h increases from 0 mm to 10 mm, then decreases from 2.301 MPa to 2.003 MPa when the horizontal spacing S_h increases from 10 mm to 20 mm. For a flaw inclination angle α of 60°, the peak strength of the specimen with S_h of 10 mm reaches 2.074 MPa, which is, respectively, 0.409 MPa and 0.168 MPa larger than for specimens with S_h of 0 mm and S_h of 20 mm.

Effects of Horizontal Spacing on the Peak Strain of Rock-Like Specimens

The peak strain of specimens containing two sets of preexisting cross flaws with different horizontal spacing under uniaxial compression is listed in **Table 3** and plotted in **Fig. 7**. The peak strain of the specimens first increases and then decreases as horizontal spacing S_h increases from 0 mm to 20 mm, as shown in **Fig. 7**. For a flaw inclination angle α of 0°, the peak strain of the specimen with $S_h = 10$ mm reaches 0.824 %, which is, respectively, 0.181 % and 0.242 % larger than for specimens with S_h of 0 mm and S_h of 20 mm. Moreover, for a flaw inclination angle α of 30°, the peak strain of the specimen with S_h of 10 mm equals 0.63 %. Compared with specimens with S_h of 0 mm and S_h of

FIG. 6

The effects of horizontal spacing on the peak strength of rock-like specimens containing preexisting cross flaws.
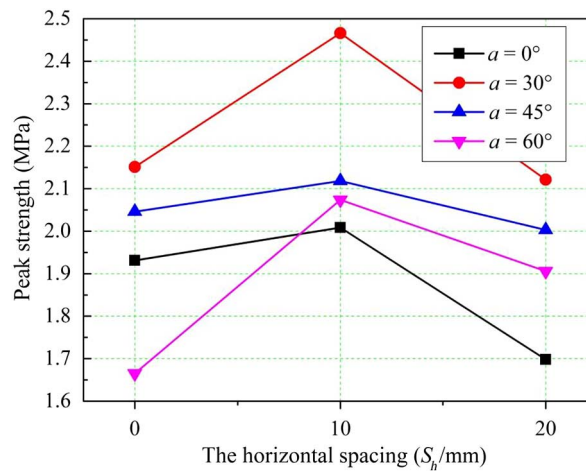

TABLE 2

The peak strengths of rock-like specimens under uniaxial compressive loads (MPa).

Horizontal Spacing (S_h, mm)	Flaw Inclination Angle (α, °)			
	0	30	45	60
0	1.931	2.151	2.046	1.665
10	2.008	2.466	2.301	2.074
20	1.646	2.121	2.003	1.906

20 mm, the peak strain of 0.63 % increases by 0.011 % and 0.127 %, respectively. For a flaw inclination angle α of 45°, the peak strain of the specimen with S_h of 10 mm reaches 0.853 % (the maximum), which is, respectively, 0.195 % and 0.2 % larger than for specimens with S_h of 0 mm and S_h of 20 mm. Finally, for a flaw inclination angle α of 60°, the peak strain of the specimen with S_h of 10 mm equals 0.722 %. Compared with specimens with S_h of 0 mm and S_h of 20 mm, the peak strain of 0.722 % increases by 0.085 %, and 0.186 %, respectively.

The Complete Axial Stress–Strain Curves of Rock-Like Specimens with the Same Horizontal Spacing

Fig. 8a shows the complete axial stress–strain curves of specimens with horizontal spacing S_h of 0 mm. The complete axial stress–strain curves include four stages: (1) the initial compaction stage, (2) the elastic stage, (3) the nonlinear hardening stage, and (4) the
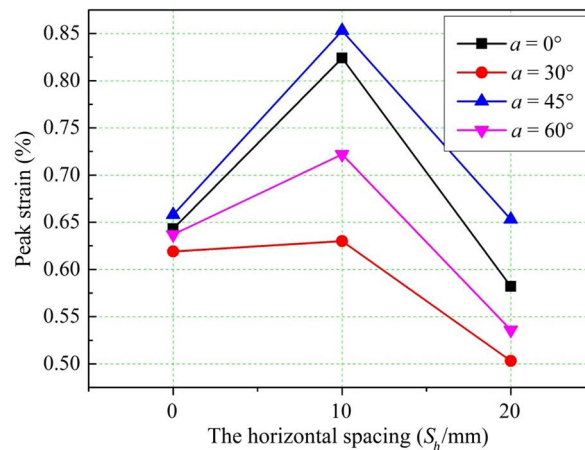
TABLE 3

The peak strain of rock-like specimens under uniaxial compressive loads (%).

Horizontal Spacing (S_h, mm)	Flaw Inclination Angle (α, °)			
	0	30	45	60
0	0.643	0.619	0.658	0.637
10	0.824	0.63	0.853	0.722
20	0.582	0.503	0.653	0.536

FIG. 7

The effects of horizontal spacing on the peak strain of rock-like specimens containing preexisting cross flaws.

strain-softening stage. Among the four specimens, the initial compaction for specimen C1 ($\alpha = 45°$) is largest, while the initial compaction for specimen D1 ($\alpha = 60°$) is smallest. The peak strength for specimen D1 ($\alpha = 60°$) is the highest (1.665 MPa), while the peak strength for specimen B1 ($\alpha = 30°$) is the lowest (2.151 MPa). Moreover, the maximum peak strain of 0.658 % among the four specimens occurs in specimen C1 ($\alpha = 45°$), whereas the minimum peak strain is 0.619 % (for specimen B1).

Fig. 8b shows the complete axial stress–strain curves of specimens with horizontal spacing S_h of 0 mm. The complete axial stress–strain curves again include four stages: (1) the initial compaction stage, (2) the elastic stage, (3) the nonlinear hardening stage, and (4) the strain-softening stage. Among the four specimens, the initial compaction for specimen A2 ($\alpha = 0°$) is the highest, while the initial compaction for specimen B2 ($\alpha = 30°$) is the lowest. Quantitatively, the peak strength for specimen A2 ($\alpha = 0°$) is the lowest (2.008 MPa), while the peak strength for specimen B2 ($\alpha = 30°$) is the highest (2.466 MPa). Moreover, the maximum peak strain of 0.853 % among the four specimens occurs in specimen C2 ($\alpha = 45°$), whereas the minimum peak strain is 0.63 % (for specimen B2).

As shown in **Fig. 8c**, the complete axial stress–strain curves of specimens with horizontal spacing S_h of 20 mm also include four stages: (1) the initial compaction stage, (2) the elastic stage, (3) the nonlinear hardening stage, and (4) the strain-softening stage. Among the four specimens, the initial compaction for specimen A3 ($\alpha = 0°$) is the highest, while the initial compaction for specimen C3 ($\alpha = 60°$) is the lowest. Quantitatively, the peak strength for specimen A3 ($\alpha = 0°$) is the lowest (1.646 MPa), while the peak strength for specimen B3 ($\alpha = 30°$) is the highest (2.121 MPa). Moreover, the maximum peak strain of 0.653 % among the four specimens occurs in specimen C3 ($\alpha = 45°$), whereas the minimum peak strain is 0.503 % (for specimen B3).

Effects of Flaw Inclination Angle on the Peak Strength of Rock-Like Specimens

Fig. 9 shows the peak strength of flawed specimens versus flaw inclination angle. The peak strength first increases, then decreases as the flaw inclination angle α increases from 0° to 60°. For a horizontal spacing S_h of 0 mm, the peak strength of a rock-like specimen with α
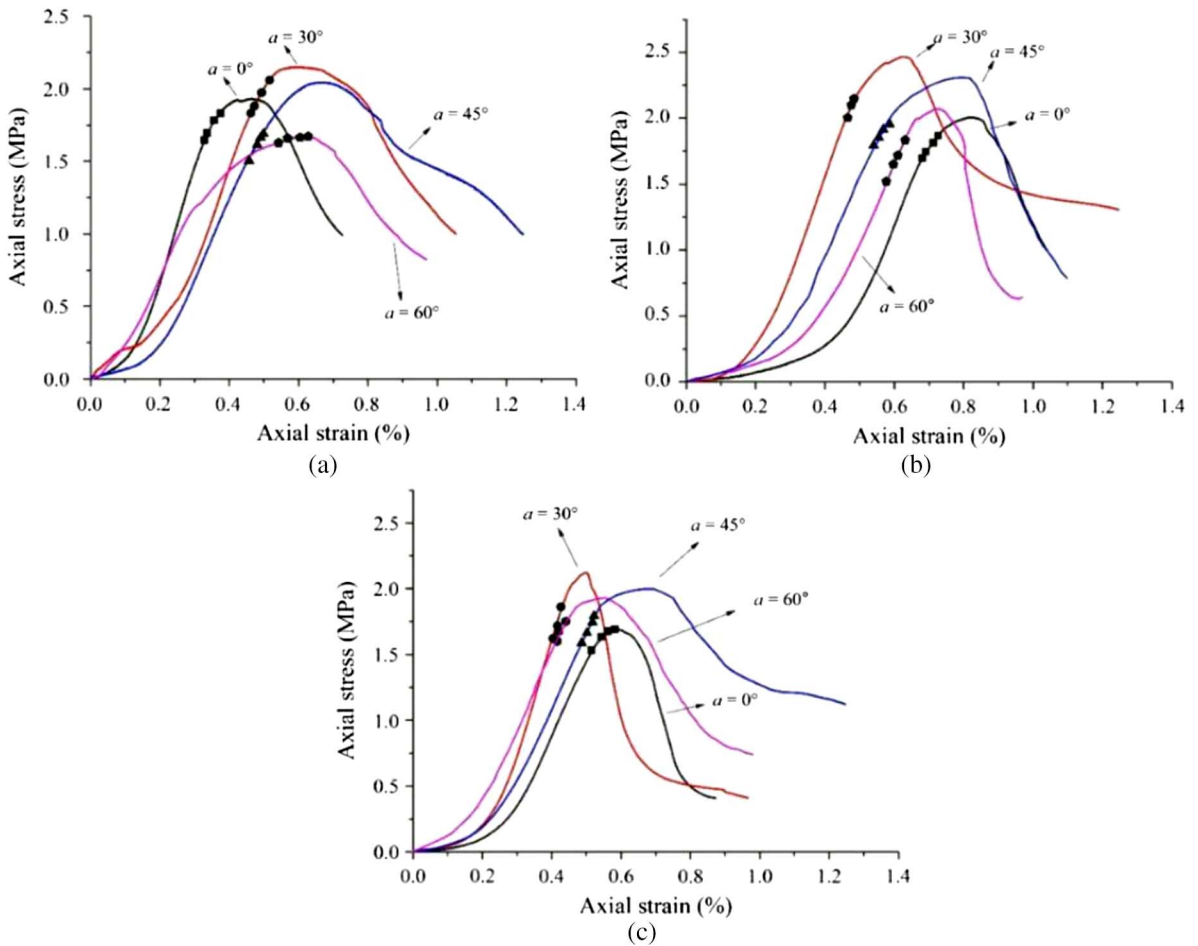
of 30° is 2.151 MPa, which is, respectively, 0.22 MPa, 0.105 MPa, and 0.486 MPa larger than for specimens with α of 0°, 45°, and 60°. For a horizontal spacing S_h of 10 mm, the peak strength of a rock-like specimen with α of 30° is 2.466 MPa, which is, respectively, 0.458 MPa, 0.165 MPa, and 0.392 MPa larger than for specimens with α of 0°, 45°, and 60°. Moreover, for a horizontal spacing S_h of 20 mm, the peak strength of a rock-like specimen with α of 30° is 2.121 MPa, which is, respectively, 0.475 MPa, 0.118 MPa, and 0.215 MPa larger than for specimens with α of 0°, 45°, and 60°.

Effects of Flaw Inclination Angle on the Peak Strain of Rock-Like Specimens

The peak strain of rock-like specimens versus flaw inclination angle is plotted in **Fig. 10**. As shown in **Fig. 10**, the peak strain first decreases, then increases, and finally decreases as the flaw inclination angle α increases from 0° to 60°. It is clear from **Fig. 10** that the peak strain always reaches the minimum value when the flaw inclination angle α is 30°, and it reaches the maximum value when the flaw inclination angle $\alpha = 45°$.

FIG. 9

The effects of flaw inclination angle on the peak strength of rock-like material specimens containing preexisting cross flaws.
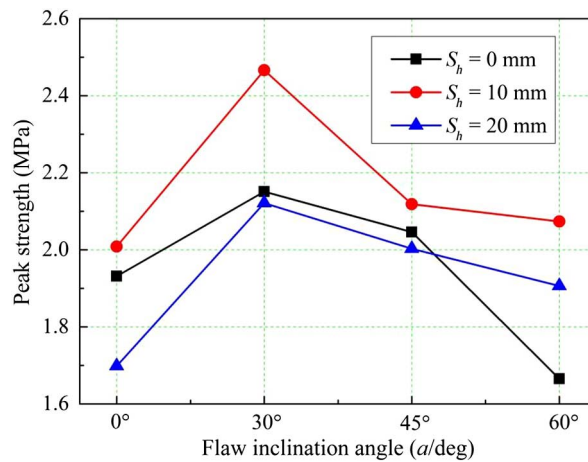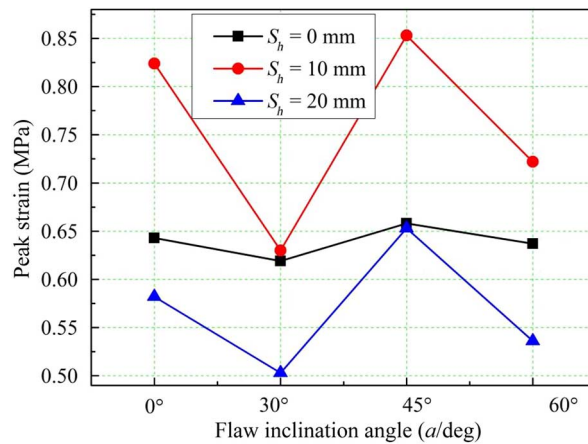

FIG. 10

Effects of flaw inclination angle on the peak strain of rock-like material specimens containing preexisting cross flaws.
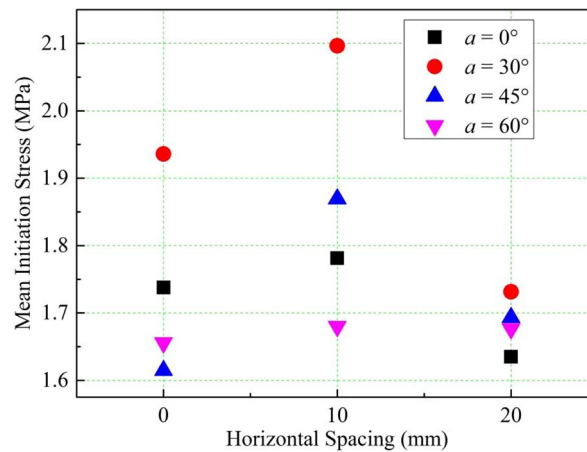

CRACK INITIATION

Effects of Horizontal Spacing on Crack Initiation Stress

The mean initiation stress is used as a representative value in this study. To investigate the effects of the horizontal spacing S_h on the crack initiation stress of the specimens, the mean crack initiation stress is plotted against the horizontal spacing S_h in **Fig. 11**. **Fig. 11** shows that the mean initiation stress first systematically increases and then decreases as the horizontal spacing S_h increases from 0 mm to 10 mm. The mean initiation stress has its maximum when $S_h = 10$ mm. For a flaw inclination angle α of 0°, the mean initiation stress of the specimen with S_h of 10 mm reaches 1.781 MPa, which is, respectively, 0.044 MPa and 0.146 MPa larger than for specimens with S_h of 0 mm and 20 mm. For a flaw inclination angle α of 30°, the mean initiation stress of the specimen with S_h of 10 mm reaches 2.096 MPa, which is, respectively, 0.16 MPa and 0.365 MPa larger than for specimens with S_h of 0 mm and 20 mm. Additionally, for a flaw inclination angle α of 45°, the mean initiation stress of the specimen with S_h of 0 mm is 1.615 MPa, and it increases to

1.869 MPa as S_h increases from 0 mm to 10 mm, then decreases from 1.869 MPa to
1.693 MPa as the horizontal spacing S_h increases from 10 mm to 20 mm. For a flaw in-
clination angle α of 60°, the mean initiation stress of the specimen with S_h of 10 mm
reaches 1.68 MPa, which is, respectively, 0.024 MPa and 0.003 MPa larger than for spec-
imens with S_h of 0 mm and S_h of 20 mm.

Effects of Flaw Inclination Angle on Crack Initiation Stress

To investigate the effects of the flaw inclination angle α on the crack initiation stress of the
specimens, the mean crack initiation stress is plotted against the flaw inclination angle α in
Fig. 12. For the rock-like specimens with horizontal spacing S_h of 10 mm and 20 mm, the
mean initiation stress first increases and then decreases as the flaw inclination angle in-
creases from 0° to 60°. The mean initiation stress is at its maximum when $\alpha = 30°$. For a
horizontal spacing S_h of 10 mm, the mean initiation stress of the specimen with α of 30°
reaches 2.096 MPa, which is, respectively, 0.315 MPa, 0.416 MPa, and 0.227 MPa larger

FIG. 12

Mean initiation stress versus
flaw inclination angle α.
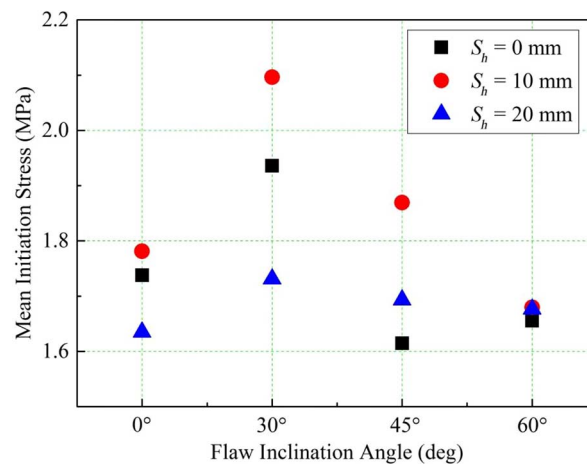
than for specimens with α of 0°, 45°, and 60°. For a horizontal spacing S_h of 20 mm, the mean initiation stress of the specimen with α of 30° reaches 1.731 MPa, which is, respectively, 0.096 MPa, 0.038 MPa, and 0.054 MPa larger than for specimens with α of 0°, 45°, and 60°. However, for the rock-like specimens with a horizontal spacing S_h of 0 mm, the mean initiation stress of the specimen with α of 30° reaches 0.936 MPa, which is, respectively, 0.198 MPa, 0.321 MPa, and 0.28 MPa larger than for specimens with α of 0°, 45°, and 60°. Note that for a horizontal spacing S_h of 0 mm, the mean initiation stress of the specimen increases from 1.614 MPa to 1.655 MPa as α increases from 45° to 60°.

Crack Initiation Mode

The ultimate failure of rock-like specimens is often related to the corresponding crack initiation [2]. This section summarizes the observed crack initiation modes, as shown in **Table 4**.

Crack Initiation Modes of Specimens with Flaw Inclination Angle of 0°

Table 4 shows that for the rock-like specimen with $\alpha = 0°$ and $S_h = 0$ mm, a wing crack is first initiated from the lower tip of flaw ②. For the specimen with α of 0° and S_h of 10 mm, a wing crack is first initiated from the right tip of flaw ①. For the specimen with α of 0° and S_h of 20 mm, a wing crack is first initiated from the right tip of flaw ①. The crack initiation modes of the specimens with a flaw inclination angle α of 0° are all wing cracks, as listed in **Table 4**. As reported by numerical works [25,40], the crack initiation mode of the flawed specimens often exhibits the initiation of wing crack.

Crack Initiation Modes of Specimens with Flaw Inclination Angle of 30°

For the rock-like specimen with $\alpha = 30°$ and $S_h = 0$ mm, a wing crack is first initiated from the left tip of flaw ①. For the rock-like specimen with α of 30° and S_h of 10 mm, a wing crack is first initiated from the right tip of flaw ②. For the rock-like specimen with α of 30° and S_h of 20 mm, a wing crack is first initiated from the right tip of flaw ②. Similarly, the crack initiation modes of the specimens with a flaw inclination angle α of 30° are all wing cracks, as listed in **Table 4**. Such experimental observations can be reproduced by a large number of numerical works, e.g., by Zhang and Wong [40] and Wang, Zhou, and Xu [41].

Crack Initiation Modes of Specimens with Flaw Inclination Angle of 45°

For the specimen with $\alpha = 45°$ and $S_h = 0$ mm, a wing crack is first initiated from the right tip of flaw ①. For the specimen with α of 45° and S_h of 10 mm, a wing crack is first initiated from the right tip of flaw ②. For the specimen with α of 45° and S_h of 20 mm, a wing crack is first initiated from the right tip of flaw ②. It is concluded that the crack initiation modes of the specimens with a flaw inclination angle α of 45° are all wing cracks, as shown in **Table 4**.

TABLE 4

Crack initiation mode in specimens under uniaxial compressive loads.

Specimen	Crack Initiation Mode
A1, A2, A3,	Wing cracks
B1, B2, B3,	
C1, C2, C3	
D1	Coplanar secondary cracks
D2	Anti-wing crack
D3	Quasi-coplanar secondary crack

Crack Initiation Modes of Specimens with Flaw Inclination Angle of 60°

For the specimen with α of 60° and S_h of 0 mm, a coplanar secondary crack is first initiated from the right tip of flaw ①. For the specimen with α of 60° and S_h of 10 mm, an anti-wing crack is first initiated from the left tip of flaw ①. For the specimen with α of 60° and S_h of 20 mm, a quasi-coplanar secondary crack is first initiated from the right tip of flaw ②. Note that the crack initiation modes of the specimens with a flaw inclination angle α of 60° are secondary cracks or anti-wing cracks, as shown in **Table 4**. It is concluded that the initiation mode transitions from wing crack to secondary crack or anti-wing crack as the flaw inclination angle increases.

CRACK COALESCENCE

Description of Crack Coalescence Process

Specimen A1 with S_h of 0 mm and α of 0°

The ultimate failure mode of specimen A1 with S_h of 0 mm and α of 0° is shown in **Fig. 13a**. When the axial stress is loaded to 1.646 MPa, wing crack A1-1-1 is first initiated from the lower tip of flaw ②, and then wing crack A1-1-2 is initiated from the upper tip of

FIG. 13   Cracking behaviors of rock-like specimen with α of 0° under uniaxial compressive loads: (a) $S_h = 0$ mm; (b) $S_h = 10$ mm; and (c) $S_h = 20$ mm.

(a) $S_h = 0$ mm, $\alpha = 0°$

(b) $S_h = 10$ mm, $\alpha = 0°$

(c) $S_h = 20$ mm, $\alpha = 0°$
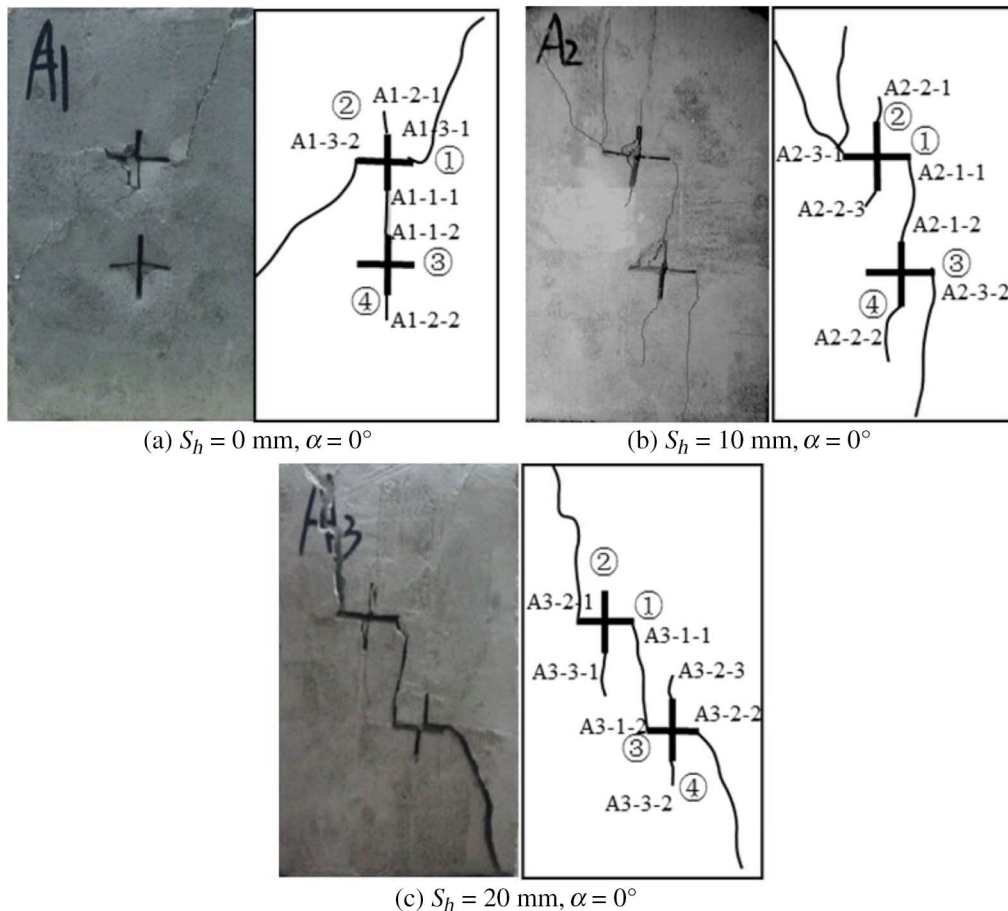
flaw ④ as the axial stress increases to 1.691 MPa. When the axial stress increases to 1.782 MPa, wing cracks A1-2-1 and A1-2-2 successively emanate from the upper tip of flaw ② and the lower tip of flaw ④. As the axial stress further increases to 1.832 MPa, the initiation of wing crack A1-1-5 and wing crack A1-1-6 occurs simultaneously. Note that no initiation behavior of flaw ③ is observed. The captured images show that wing cracks, labeled A1-1-1, A1-1-2, A1-2-1, and A1-2-2, propagate along the loading direction, while wing cracks A1-3-1 and A1-3-2 grow toward the lateral boundary. The growth of the former four wing cracks normally follows a smooth path, while the growth of the latter two wing cracks follows a curvilinear path. Wing crack A1-1-1 emanating from the lower tip of flaw ② ultimately coalesces with wing crack A1-1-2 emanating from the upper tip of flaw ④ as the axial stress continues to increase. It is worth noting that wing cracks A1-3-1 and A1-3-2 continue to propagate until they reach the lateral boundary of specimen A1, which leads to the ultimate failure of the specimen. The cracks observed in specimen A1 under uniaxial compressive loads are shown in **Table 5**.

Specimen A2 with S_h of 10 mm and α of 0°

The ultimate failure mode of specimen A2 with S_h of 10 mm and α of 0° is shown in **Fig. 13b**. When the axial stress is loaded to 1.697 MPa, wing crack A2-1-1 is first initiated from the right tip of flaw ①, and then wing crack A2-1-2 is initiated from the upper tip of flaw ④ as the load increases to 1.746 MPa. When the axial stress increases to 1.814 MPa, wing cracks A2-2-1, A2-2-2, and A2-2-3 successively emanate from the upper tip of flaw ②, the lower tip of flaw ④, and the lower tip of flaw ②. When the axial stress is loaded to 1.868 MPa, wing cracks A2-3-1 and A2-3-2 are finally initiated at a similar stress level. The captured images show that wing cracks A2-1-1, A2-1-2, A2-2-1, A2-2-2, and A2-3-2 propagate along the loading direction, while wing crack A2-3-1 propagates toward the left boundary of the specimen. The growth of the former five wing cracks follows a smooth path, while the growth of the latter one follows a curvilinear path. As the compressive load increases further, wing crack A2-1-1 emanating from the right tip of flaw ① coalesces with wing crack A2-1-2 emanating from the upper tip of flaw ④. The cracks observed in specimen A2 under uniaxial compressive loads are listed in **Table 6**.

Specimen A3 with S_h of 20 mm and α of 0°

The ultimate failure mode of specimen A3 with S_h of 20 mm and α of 0° is shown in **Fig. 13c**. First, wing crack A3-1-1 is initiated from the right tip of flaw ① when the axial stress is loaded to 1.534 MPa, and wing crack A3-1-2 is initiated from the left tip of flaw ③ as the load reaches 1.636 MPa. Wing cracks A3-2-1, A3-2-2, and A3-2-3 are initiated from the left tip of flaw ①, the right tip of flaw ③, and the upper tip of flaw ④ when the axial stress

TABLE 5

Cracks in specimen A1 under uniaxial compressive loads.

Crack Sequence	Crack Type
Crack A1-1-1	Wing crack
Crack A1-1-2	Wing crack
Crack A1-2-1	Wing crack
Crack A1-2-2	Wing crack
Crack A1-3-1	Wing crack
Crack A1-3-2	Wing crack

TABLE 6
Cracks in specimen A2 under uniaxial compressive loads.

Crack Sequence	Crack Type
Crack A2-1-1	Wing crack
Crack A2-1-2	Wing crack
Crack A2-2-1	Wing crack
Crack A2-2-2	Wing crack
Crack A2-2-3	Wing crack
Crack A2-3-1	Wing crack
Crack A2-3-2	Wing crack

increases to 1.678 MPa. When the axial stress is loaded to 1.692 MPa, wing cracks A3-3-1 and A3-3-2 successively emanate from the lower tip of flaw ② and flaw ④. Note that wing crack A3-2-2 propagates toward the bottom boundary of the specimen, while the other wing cracks propagate along the loading direction in a smooth path. There is no further extension after wing cracks A3-2-3 and A3-3-2 are initiated. As the compressive load increases further, wing crack A3-1-1 emanating from the right tip of flaw ① coalesces with wing crack A3-1-2 emanating from the left tip of flaw ③. The cracks observed in specimen A3 under uniaxial compressive loads are listed in **Table 7**.

Specimen B1 with S_h of 0 mm and α of 30°

Fig. 14a shows the ultimate failure mode of specimen B1 with S_h of 0 mm and α of 30°. When the axial stress reaches 1.830 MPa, wing cracks B1-1-1 and B1-1-2 are respectively initiated from the left tip of flaw ① and near the left tip of flaw ④. Note that anti-wing crack B1-2-1 is initiated from the right tip of flaw ④ as the load increases to 1.881 MPa. When the axial stress is loaded to 1.973 MPa, the quasi-coplanar secondary crack B1-2-2, wing crack B1-3-1 and coplanar secondary crack B1-3-2 successively emanate from the left tip of flaw ②, the left tip of flaw ③, and the right tip of flaw ②. The captured images show that wing cracks B1-1-1, B1-1-2, and B1-3-1 propagate along the loading direction, while the growth of quasi-coplanar secondary crack B1-2-2 and coplanar secondary crack B1-3-2 propagate toward the top and right boundaries of the specimen in a curvilinear path, respectively. Wing crack B1-1-1 emanating from the left tip of flaw ① finally coalesces with wing crack B1-1-2 emanating from the left tip of flaw ④ as the axial stress continues to increase. Next, the coalescence of cracks continues through the linkage of anti-wing crack B1-2-1 and coplanar secondary crack B1-3-2. The cracks observed in specimen B1 under uniaxial compressive loads are listed in **Table 8**.

TABLE 7
Cracks in specimen A3 under uniaxial compressive loads.

Crack Sequence	Crack Type
Crack A3-1-1	Wing crack
Crack A3-1-2	Wing crack
Crack A3-2-1	Wing crack
Crack A3-2-2	Wing crack
Crack A3-2-3	Wing crack
Crack A3-3-1	Wing crack
Crack A3-3-2	Wing crack

FIG. 14 Cracking behaviors of rock-like specimen with α of 30° under uniaxial compressive loads: (a) $S_h = 0$ mm; (b) $S_h = 10$ mm; and
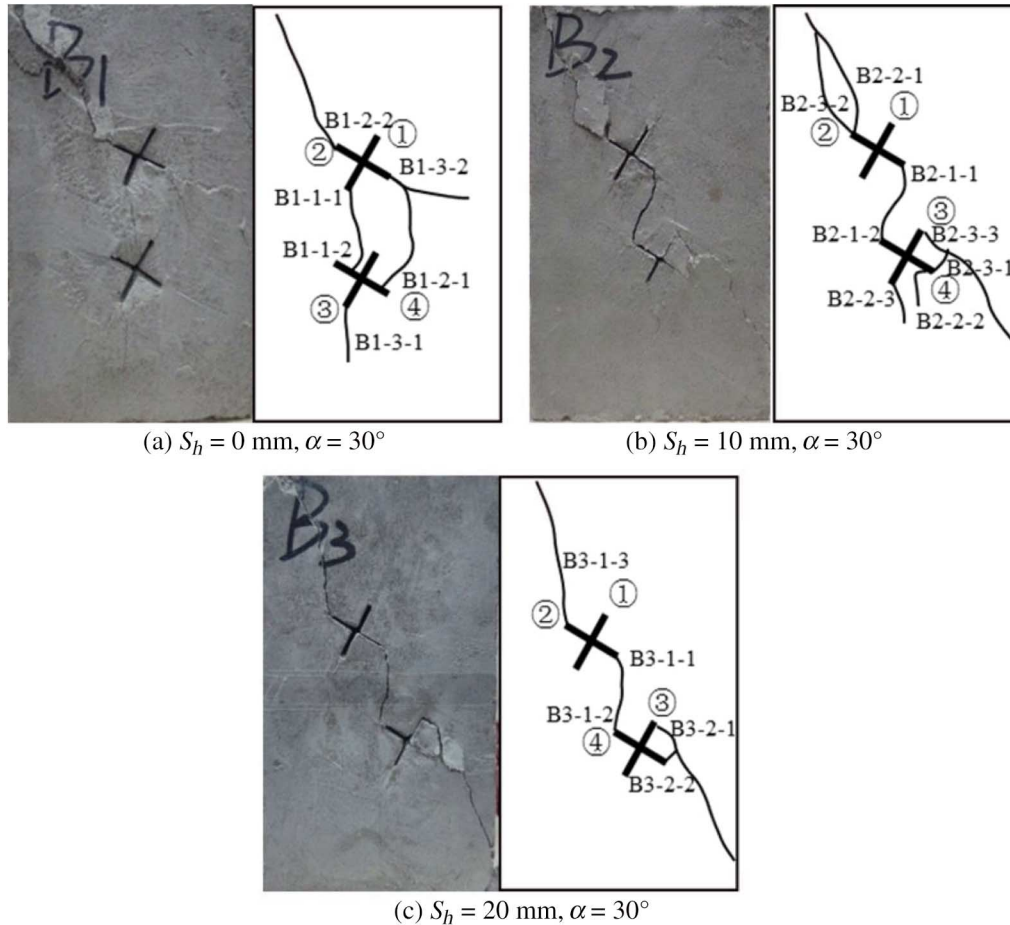(c) $S_h = 20$ mm.

(a) $S_h = 0$ mm, $\alpha = 30°$

(b) $S_h = 10$ mm, $\alpha = 30°$

(c) $S_h = 20$ mm, $\alpha = 30°$

TABLE 8
Cracks in specimen B1 under uniaxial compressive loads.

Crack Sequence	Crack Type
Crack B1-1-1	Wing crack
Crack B1-1-2	Wing crack
Crack B1-2-1	Anti-wing crack
Crack B1-2-2	Quasi-coplanar secondary crack
Crack B1-3-1	Wing crack
Crack B1-3-2	Coplanar secondary crack

Specimen B2 with S_h of 10 mm and α of 30°

Fig. 14b shows the ultimate failure mode of specimen B2 with S_h of 10 mm and α of 30°.
When the axial stress is loaded to 2.004 MPa, wing crack B2-1-1 is first initiated from the
right tip of flaw ②, and then wing crack B2-1-2 is initiated from the left tip of flaw ④ as the

load increases to 2.137 MPa. As the axial stress increases to 2.148 MPa, wing cracks B2-2-1, B2-2-2, and B2-2-3 successively emanate from the left tip of flaw ②, the right tip of flaw ④, and the left tip of flaw ③. Finally, anti-wing crack B2-3-1, quasi-coplanar secondary crack B2-3-2, and oblique secondary crack B2-3-3 emanate at a similar stress level. Note that no initiation behavior of flaw ① is observed. The captured images show that wing crack B2-2-1 and quasi-coplanar secondary crack B2-3-2 propagate toward the top boundary of the specimen, while oblique secondary crack B2-3-3 propagates toward the right boundary of the specimen in a curvilinear path. Wing crack B2-1-1 emanating from the lower tip of flaw ① eventually coalesces with wing crack B2-1-2 emanating from the left tip of flaw ④ when the axial stress continues to increase. The coalescence continues through the linkage of anti-wing crack B2-3-1 and oblique secondary crack B2-3-3. The cracks observed in specimen B2 under uniaxial compressive loads are listed in **Table 9**.

Specimen B3 with S_h of 20 mm and α of 30°

Fig. 14c shows the ultimate failure mode of specimen B3 with S_h of 20 mm and α of 30°. When the axial stress is loaded to 1.614 MPa, wing cracks B3-1-1, B3-1-2, and B3-1-3 are respectively initiated from the right tip of flaw ②, the left tip of flaw ④, and the left tip of flaw ②. Oblique secondary crack B3-2-1 and anti-wing crack B3-2-2 successively emanate from the right tip of flaw ③ and the right tip of flaw ④ when the axial stress increases to 1.718 MPa. However, no initiation behavior of flaw ① is observed. The captured images show that wing crack B3-1-3 propagates toward the top boundary of the specimen, while oblique secondary crack B3-2-1 propagates toward the right boundary of specimen until the failure of specimen appears. Meanwhile, wing cracks B3-1-1 and B3-1-2 propagate along the loading direction within the ligament zone. The first coalescence occurs through the linkage of wing cracks B3-1-1 and B3-1-2, and the other coalescence of oblique secondary crack B3-2-1 and anti-wing crack B3-2-2 occurs as the load increases. The cracks observed in specimen B3 under uniaxial compressive loads are listed in **Table 10**.

Specimen C1 with S_h of 0 mm and α of 45°

Fig. 15a shows the ultimate failure mode of specimen C1 with S_h of 0 mm and α of 45°. The captured images show that wing crack C1-1-1 is first initiated from the right tip of flaw ① when the axial stress reaches 1.5 MPa, and then wing cracks C1-1-2 and C1-1-3 are initiated from the right tips of flaw ② and flaw ③ as the load increases to 1.615 MPa. As the axial stress increases further to 1.664 MPa, coplanar secondary crack C1-2-1 and wing crack C1-2-2 are successively initiated from the left tip of flaw ④ and the right tip of

TABLE 9

Cracks in specimen B2 under uniaxial compressive loads.

Crack Sequence	Crack Type
Crack B2-1-1	Wing crack
Crack B2-1-2	Wing crack
Crack B2-2-1	Wing crack
Crack B2-2-2	Wing crack
Crack B2-2-3	Wing crack
Crack B2-3-1	Anti-wing crack
Crack B2-3-2	Quasi-coplanar secondary crack
Crack B2-3-3	Oblique secondary crack

TABLE 10
Cracks in specimen B3 under uniaxial compressive loads.

Crack Sequence	Crack Type
Crack B3-1-1	Wing crack
Crack B3-1-2	Wing crack
Crack B3-1-3	Wing crack
Crack B3-2-1	Oblique secondary crack
Crack B3-2-2	Anti-wing crack

flaw ④. When the axial stress reaches 1.680 MPa, quasi-coplanar secondary crack C1-3-1 and oblique secondary crack C1-3-2 are initiated at a similar stress level. Additionally, the captured images show that wing cracks C1-1-1, C1-1-2, C1-1-3, and C1-2-2 propagate along the loading direction, while quasi-coplanar secondary crack C1-3-1 and oblique secondary crack C1-3-2 propagate toward the top and bottom boundaries of the specimen in a curvilinear path, respectively. Wing crack C1-1-2 finally coalesces with wing crack

FIG. 15 Cracking behaviors of rock-like specimen with α of 45° under uniaxial compressive loads: (a) $S_h = 0$ mm; (b) $S_h = 10$ mm; and (c) $S_h = 20$ mm.
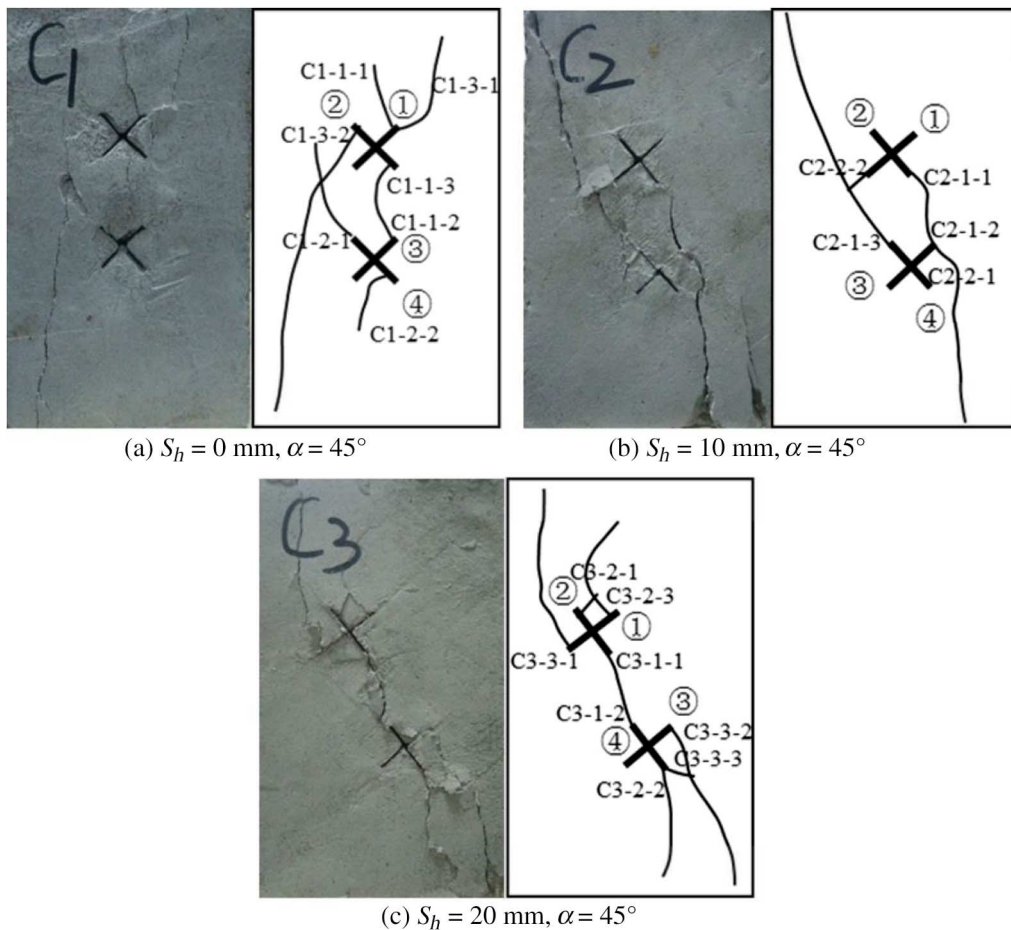

(a) $S_h = 0$ mm, $\alpha = 45°$

(b) $S_h = 10$ mm, $\alpha = 45°$

(c) $S_h = 20$ mm, $\alpha = 45°$

TABLE 11

Cracks in specimen C1 under uniaxial compressive loads.

Crack Sequence	Crack Type
Crack C1-1-1	Wing crack
Crack C1-1-2	Wing crack
Crack C1-1-3	Wing crack
Crack C1-2-1	Coplanar secondary crack
Crack C1-2-2	Wing crack
Crack C1-3-1	Quasi-coplanar secondary crack
Crack C1-3-2	Oblique secondary crack

C1-1-3, and then the next coalescence occurs through the linkage of coplanar secondary crack C1-2-1 and oblique secondary crack C1-3-2 as the compressive loads continue to increase. The cracks observed in specimen C1 under uniaxial compressive loads are listed in **Table 11**.

Specimen C2 with S_h of 10 mm and α of 45°

The ultimate failure mode of specimen C2 with S_h of 10 mm and α of 45° is shown in **Fig. 15b**. When the axial stress is loaded to 1.794 MPa, wing crack C2-1-1 is first initiated from the right tip of flaw ②, and then wing crack C2-1-2 and coplanar secondary crack C2-1-3 are initiated from the right tip of flaw ③ and the left tip of flaw ④ in turn as the load increases to 1.806 MPa. Finally, oblique secondary crack C2-2-1 and coplanar secondary crack C2-2-2 are, respectively, initiated from the right tip of flaw ③ and the left tip of flaw ① when the load reaches 1.956 MPa. The captured images show that wing cracks C2-1-1 and C2-1-2 propagate along the loading direction, while coplanar secondary crack C2-1-3 and oblique secondary crack C2-2-1 propagate towards the top and bottom boundaries of the specimen in a curvilinear path. The first coalescence occurs through the linkage of wing cracks C2-1-1 and C2-1-2, and the second coalescence of coplanar secondary crack C2-1-3 and coplanar secondary crack C2-2-2 occurs as the compressive load continues to increase. The cracks observed in specimen C2 under uniaxial compressive loads are listed in **Table 12**.

Specimen C3 with S_h of 20 mm and α of 45°

Fig. 15c shows the ultimate failure mode of specimen C3 with S_h of 20 mm and α of 45°. When the axial stress is loaded to 1.588 MPa, wing crack C3-1-1 is first initiated from the right tip of flaw ②, and then wing crack C3-1-2 is initiated from the left tip of flaw ④ as the load increases to 1.664 MPa. As the load increases to 1.746 MPa, wing cracks C3-2-1,

TABLE 12

Cracks in specimen C2 under uniaxial compressive loads.

Crack Sequence	Crack Type
Crack C2-1-1	Wing crack
Crack C2-1-2	Wing crack
Crack C2-1-3	Coplanar secondary crack
Crack C2-2-1	Oblique secondary crack
Crack C2-2-2	Coplanar secondary crack

TABLE 13

Cracks in specimen C3 under uniaxial compressive loads.

Crack Sequence	Crack Type
Crack C3-1-1	Wing crack
Crack C3-1-2	Wing crack
Crack C3-2-1	Wing crack
Crack C3-2-2	Wing crack
Crack C3-2-3	Wing crack
Crack C3-3-1	Anti-wing crack
Crack C3-3-2	Anti-wing crack
Crack C3-3-3	Quasi-coplanar secondary crack

C3-2-2, and C3-2-3 successively emanate from the left tip of flaw ②, the right tip of flaw ④, and the right tip of flaw ①. When the axial stress reaches 1.775 MPa, anti-wing cracks C3-3-1 and C3-3-2 and quasi-coplanar secondary crack C3-3-3 successively emanate from the left tip of flaw ①, the right tip of flaw ③. and the right tip of flaw ④. From the captured images, wing crack C3-1-1 emanating from the right tip of flaw ② first coalesces with wing crack C3-1-2 emanating from the left tip of flaw ④ as the compressive load continues to increase. Then, the second coalescence occurs through the linkage of wing cracks C3-2-1 and C3-2-3, and finally the coalescence of anti-wing crack C3-3-2 and quasi-coplanar secondary crack C3-3-3 occurs. The cracks observed in specimen C3 under uniaxial compressive loads are listed in **Table 13**.

Specimen D1 with S_h of 0 mm and α of 60°

The ultimate failure mode of specimen D1 with S_h of 0 mm and α of 60° is shown in **Fig. 16a**. When the axial stress is loaded to 1.628 MPa, coplanar secondary crack D1-1-1 is first initiated from the right tip of flaw ①. As the load increases to 1.659 MPa, coplanar secondary crack D1-1-2 and wing crack D1-1-3 are initiated from the left tip of flaw ④ and near the left tip of flaw ①, respectively. When the axial stress increases to 1.672 MPa, wing cracks D1-2-1, D1-2-2, and D1-3-1 successively emanate from the left tip of flaw ③, the right tip of flaw ④, and the left tip of flaw ②. The captured images show that wing cracks D1-1-1, D1-1-2, and D1-2-1 propagate along the loading direction in a smooth path, while coplanar secondary crack D1-1-1 propagates toward the top boundary of the specimen. Coplanar secondary crack D1-1-2 emanating from the upper tip of flaw ④ finally coalesces with wing crack D1-1-3 emanating from the left tip of flaw ① as the axial stress continues to increase. It is worth noting that coplanar secondary crack D1-1-1 and wing crack D1-2-1 continue to propagate until they reach the top and bottom boundaries of the specimen, respectively. Note that coplanar secondary crack D1-1-2 coalesces with the preexisting flaw ①. The cracks observed in specimen D1 under uniaxial compressive loads are listed in **Table 14**.

Specimen D2 with S_h of 10 mm and α of 60°

The ultimate failure mode of specimen D2 with S_h of 10 mm and α of 60° is shown in **Fig. 16b**. When the axial stress is loaded to 1.52 MPa, anti-wing crack D2-1-1 is initiated from the left tip of flaw ① and propagates toward the top boundary of the specimen. Next, wing crack D2-2-1 is initiated from the lower tip of flaw ②, and quasi-coplanar secondary crack D2-2-2 is initiated from the upper tip of flaw ④. As the load increases to 1.832 MPa,

FIG. 16   Cracking behaviors of rock-like specimen with α of 60° under uniaxial compressive loads: (a) $S_h = 0$ mm, $\alpha = 60°$; (b) $S_h = 10$ mm, $\alpha = 60°$; and (c) $S_h = 20$ mm, $\alpha = 60°$.
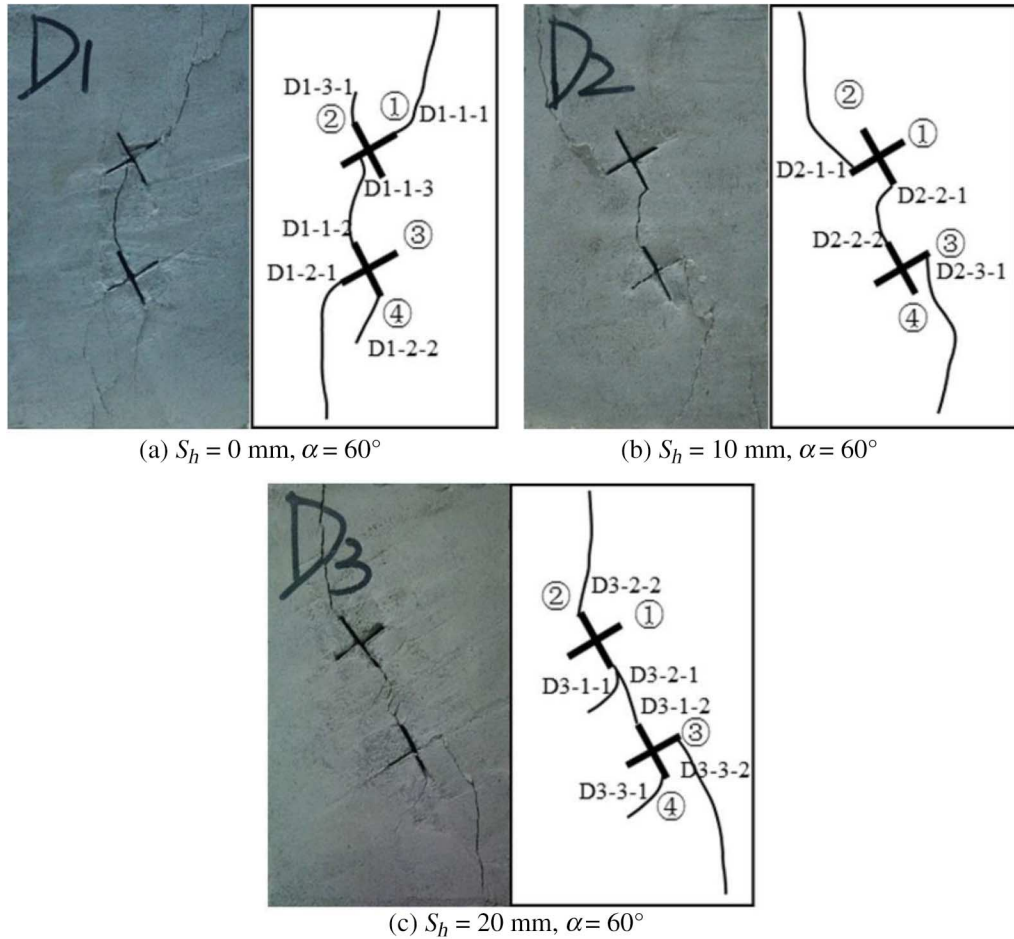

(a) $S_h = 0$ mm, $\alpha = 60°$ (b) $S_h = 10$ mm, $\alpha = 60°$

(c) $S_h = 20$ mm, $\alpha = 60°$

TABLE 14

Cracks in specimen D1 under uniaxial compressive loads.

Crack Sequence	Crack Type
Crack D1-1-1	Coplanar secondary crack
Crack D1-1-2	Coplanar secondary crack
Crack D1-1-3	Wing crack
Crack D1-2-1	Wing crack
Crack D1-2-2	Wing crack
Crack D1-3-1	Wing crack

oblique secondary crack D2-3-1 is initiated from the right tip of flaw ③ and propagates toward the bottom boundary of the specimen until failure of the specimen occurs. Note that quasi-coplanar secondary crack D2-2-2 coalesces with wing crack D2-2-1 in this specimen. The cracks observed in specimen D2 under uniaxial compressive loads are listed in **Table 15**.

TABLE 15
Cracks in specimen D2 under uniaxial compressive loads.

Crack Sequence	Crack Type
Crack D2-1-1	Anti-wing crack
Crack D2-2-1	Wing crack
Crack D2-2-2	Quasi-coplanar secondary crack
Crack D2-3-1	Oblique secondary crack

Specimen D3 with S_h of 20 mm and α of 60°

Fig. 16c shows the ultimate failure mode of specimen D3 with S_h of 20 mm and α of 60°. When the axial stress is loaded to 1.602 MPa, quasi-coplanar secondary crack D3-1-1 is first initiated from the right tip of flaw ②, and after that, coplanar secondary crack D3-1-2 is quickly initiated from the left tip of flaw ④ and finally coalesces with coplanar secondary crack D3-2-1 emanating from the right tip of flaw ②. As the load reaches 1.676 MPa, wing cracks D3-2-2 and D3-3-1 are respectively initiated from the left tip of flaw ② and the right tip of flaw ④ at a similar stress level. When the axial stress is loaded to 1.752 MPa, anti-wing crack D3-3-2 is finally initiated from the right tip of flaw ③ and propagates toward the bottom boundary of specimen. Captured images show that wing crack D3-2-2 grow along the loading direction in a smooth path. Note that coplanar secondary crack D3-2-1 coalesces with coplanar secondary crack D3-1-2, and there is no linkage among wing cracks in this specimen. The cracks observed in specimen D3 subjected to uniaxial compressive loads are listed in **Table 16**.

Summary of Crack Coalescence Type

As illustrated in **Table 17**, seven types of crack coalescence in rock-like specimens containing two sets of preexisting cross flaws are observed: type I, coalescence of wing cracks; type II, coalescence of wing crack and coplanar secondary crack; type III, coalescence of wing crack and quasi-coplanar secondary crack; type IV, coalescence of anti-wing crack and quasi-coplanar secondary crack; type V, coalescence of anti-wing cracks; type VI, coalescence of anti-wing crack and coplanar secondary crack; and type VII, coalescence of coplanar secondary cracks. It is found from these seven types of crack coalescence that a set of preexisting flaws coalesce not only with another set of preexisting flaws but also with the identical set of preexisting flaws. More specifically, type I of crack coalescence belongs to the crack coalescence between a set of preexisting flaws and another set of preexisting flaws, along with type II, type III, type IV, and type VII of crack coalescence. Then, type V and type VI of crack coalescence belong to the crack coalescence between the double
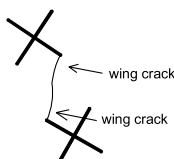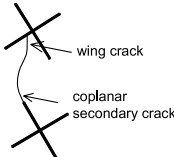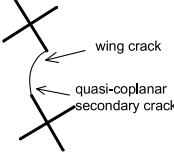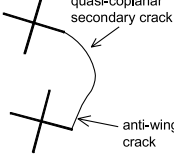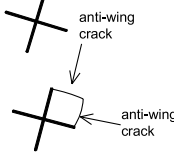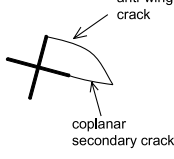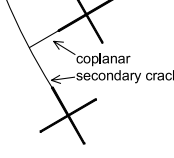
TABLE 16
Cracks in specimen D3 under uniaxial compressive loads.

Crack Sequence	Crack Type
Crack D3-1-1	Quasi-coplanar secondary crack
Crack D3-1-2	Coplanar secondary crack
Crack D3-2-1	Coplanar secondary crack
Crack D3-2-2	Wing crack
Crack D3-3-1	Wing crack
Crack D3-3-2	Anti-wing crack

TABLE 17

The coalescence type of rock-like material specimens containing preexisting cross flaws.

Crack Coalescence Type	Sketch of Crack Coalescence	Description of Crack Coalescence Type	Occurrence Frequency in the Present Experiment	Specimens
Coalescence type I	wing crack / wing crack	Coalescence of two wing cracks	9	A1,A2,A3; B1,B2,B3; C1,C2,C3
Coalescence type II	wing crack / coplanar secondary crack	Coalescence of wing crack and coplanar secondary crack	1	D1
Coalescence type III	wing crack / quasi-coplanar secondary crack	Coalescence of wing crack and quasi-coplanar secondary crack	1	D2
Coalescence type IV	quasi-coplanar secondary crack / anti-wing crack	Coalescence of anti-wing crack and quasi-coplanar secondary crack	2	B1; C1
Coalescence type V	anti-wing crack / anti-wing crack	Coalescence of two anti-wing cracks	2	B2; C3
Coalescence type VI	anti-wing crack / coplanar secondary crack	Coalescence of anti-wing crack and coplanar secondary crack	1	B3
Coalescence type VII	coplanar secondary crack	Coalescence of two coplanar secondary cracks	3	C2,C3; D3

preexisting cross flaws within the same set. Among these seven types of crack coalescence, type I, i.e., the coalescence of wing cracks, is the most common, accounting for 47.4 % of all of the coalescences. According to the statistics on the types of crack coalescence, the coalescence of wing cracks or the coalescence of a wing crack with other types of cracks accounts for 57.9 % of all coalescence. Note that type VII crack coalescence is observed in three specimens, i.e., specimen C2 ($\alpha = 45°$, $S_h = 10$ mm), specimen C3 ($\alpha = 45°$,

$S_h = 20$ mm), and specimen D3 ($\alpha = 60°$, $S_h = 20$ mm). Type II is only observed once, whereas type IV occurs twice in the experiment. Moreover, type I crack coalescence is not observed in specimens with α of 60°.

To our best knowledge, a large number of numerical studies on the crack coalescence of two, three, or multiple preexisting flaws were performed previously [8,25,40–45]. These previous works can provide the numerical verification for this present experimental study. Almost all types of crack coalescence, as shown in **Table 17**, were reproduced and reported by these numerical works. As observed from the present laboratory experiment, the coalescences of two wing cracks, anti-wing crack and quasi-coplanar secondary crack, wing crack and quasi-coplanar secondary crack, often occur in the numerical simulations. For example, the coalescence of two wing cracks was reported by Zhang and Wong [40], who used the Bonded-Particle Model to simulate double flaw-contained specimens under uniaxial compression. Such a type of crack coalescence was also reported by Zhou, Bi, and Qian [42], who conducted General Particle Dynamics numerical experiments on rock-like specimens containing multiple preexisting flaws. Zhou, Bi, and Qian [42] also reported the coalescence of wing crack and quasi-coplanar secondary crack, namely, type III of crack coalescence observable in this experiment. Moreover, the coalescence of anti-wing crack and quasi-coplanar secondary crack (type IV of crack coalescence) was reported by Haeri [43], who used the Higher Order Displacement Discontinuity Method to investigate the growth of neighboring cracks in rock-like cylindrical specimens containing three preexisting flaws under uniaxial compression. The coalescence of wing crack and quasi-coplanar secondary crack, namely, type III of crack coalescence, was reproduced by the peridynamics method [41], as well as the coalescence of two wing cracks (type I of crack coalescence) and the coalescence of anti-wing crack and quasi-coplanar secondary crack (type IV of crack coalescence). However, two types of crack coalescence occurring within the same set were rarely reported by the previous numerical works. This is because uniaxial compressive experiments were seldom conducted numerically on specimens containing preexisting cross flaws. The present study provides the experimental basis for the future pursuit of related numerical study, which can in turn help verify the experimental results and reveal the underlying fracture mechanism.

Conclusions

Uniaxial compression tests of rock-like specimens containing two sets of preexisting cross flaws are performed in this study. These experiments mainly focus on the effects of the flaw inclination angle and the horizontal spacing on the mechanical and cracking behaviors of rock-like specimens. The real-time cracking process in specimens with different horizontal spacings and flaw inclination angles is investigated. This study provides a better understanding of the cracking behaviors of two sets of preexisting cross flaws, corresponding to those natural flaws that appear in sets or groups with similar orientation and characteristics in real rock engineering. The following conclusions can be drawn:

(1) Five types of cracks, namely, wing crack, anti-wing crack, coplanar secondary crack, quasi-coplanar secondary crack, and oblique secondary crack, are found in specimens containing two sets of preexisting cross flaws.
(2) The crack initiation modes depend strongly on the inclination angle rather than the horizontal spacing. The crack initiation mode of the specimens is secondary cracks

when flaw inclination angle $\alpha = 60°$, while the crack initiation mode of the specimens is wing cracks when $\alpha < 60°$.

(3) The mean initiation stress of the specimens is significantly affected by the geometry of preexisting cross flaws. For specimens with horizontal spacing of 10 mm and 20 mm, the mean initiation stress first increases and then decreases as the flaw inclination angle increases from 0° to 60°, and it reaches its maximum in specimens with the flaw inclination angle of 30°. However, for specimens with a horizontal spacing of 0 mm, the mean initiation stress first increases, then decreases, and finally increases as the flaw inclination angle increases from 0° to 60°. For a fixed flaw inclination angle, the mean initiation stress first increases and then decreases as the horizontal spacing increases from 0 mm to 20 mm, and it reaches its maximum in specimens with the horizontal spacing of 10 mm.

(5) Seven types of coalescence are observed in specimens containing two sets of preexisting cross flaws: (a) coalescence of wing cracks; (b) coalescence of wing crack and coplanar secondary crack; (c) coalescence of wing crack and quasi-coplanar secondary crack; (d) coalescence of anti-wing crack and quasi-coplanar secondary crack; (e) coalescence of anti-wing cracks; (f) coalescence of anti-wing crack and coplanar secondary crack; and (g) coalescence of coplanar secondary cracks.

(6) Complete stress–strain curves include four stages, i.e., the initial compaction stage, elastic deformation stage, nonlinear hardening stage, and strain-softening stage. The peak strength and peak strain first increase and then decrease as the horizontal spacing increases. Meanwhile, the peak strength first increases and then decreases, and the peak strain first decreases, then increases, and finally decreases as the flaw inclination angle increases.

References

[1] Li, Y. P., Chen, L. Z., and Wang, Y. H., "Experimental Research on Pre-cracked Marble under Compression," *Int. J. Solids Struct.*, Vol. 42, Nos. 9–10, 2005, pp. 2505–2516, https://doi.org/10.1016/j.ijsolstr.2004.09.033

[2] Zhou, X. P., Cheng, H., and Feng, Y. F., "An Experimental Study of Crack Coalescence Behaviour in Rock-Like Materials Containing Multiple Flaws under Uniaxial Compression," *Rock Mech. Rock Eng.*, Vol. 47, No. 6, 2014, pp. 1961–1986, https://doi.org/10.1007/s00603-013-0511-7

[3] Wong, L. N. Y. and Zhang, X. P., "Size Effects on Cracking Behavior of Flaw-Containing Specimens under Compressive Loading," *Rock Mech. Rock Eng.*, Vol. 47, No. 5, 2014, pp. 1921–1930, https://doi.org/10.1007/s00603-013-0424-5

[4] Cao, P., Liu, T., Pu, C., and Lin, H., "Crack Propagation and Coalescence of Brittle Rock-Like Specimens with Pre-Existing Cracks in Compression," *Eng. Geol.*, Vol. 187, 2015, pp. 113–121, https://doi.org/10.1016/j.enggeo.2014.12.010

[5] Wong, L. N. Y., Zou, C. J., and Cheng, Y., "Fracturing and Failure Behavior of Carrara Marble in Quasistatic and Dynamic Brazilian Disc Tests," *Rock Mech. Rock Eng.*, Vol. 47, No. 4, 2014, pp. 1117–1133, https://doi.org/10.1007/s00603-013-0465-9

[6] Haeri, H., Shahriar, K., Marji, M. F., and Moarefvand, P., "Experimental and Numerical Study of Crack Propagation and Coalescence in Pre-Cracked Rock-Like Disks," *Int. J. Rock Mech. Min. Sci.*, Vol. 67, No. 4, 2014, pp. 20–28.

[7] Wong, R. H. C. and Chau, K. T., "Crack Coalescence in a Rock-Like Material Containing Two Cracks," *Int. J. Rock Mech. Min. Sci.*, Vol. 35, No. 2, 1998, pp. 147–164, https://doi.org/10.1016/S0148-9062(97)00303-3

[8] Tang, C. A., Lin, P., Wong, R. H. C., and Chau, K. T., "Analysis of Crack Coalescence in Rock-Like Materials Containing Three Flaws—Part II: Numerical Approach," *Int. J. Rock Mech. Min. Sci.*, Vol. 38, No. 7, 2001, pp. 925–939, https://doi.org/10.1016/S1365-1609(01)00065-X

[9] Zhang, J. Z., Yu, J., Cai, Y. Y., Chen, S. H., and Lin, C. M., "Visco-Elastic-Plastic Creep Solutions and Deformation Properties of Tunnels in Swelling Rocks under Seepage," *Chin. J. Geotech. Eng.*, Vol. 36, No. 12, 2014, pp. 2195–2202.

[10] Wong, L. N. Y., Li, Z. H., Kang, H. M., and Teh, C. I., "Dynamic Loading of Carrara Marble in a Heated State," *Rock Mech. Rock Eng.*, Vol. 50, No. 6, 2017, pp. 1487–1505, https://doi.org/10.1007/s00603-017-1170-x

[11] Havaej, M., Coggan, J., Stead, D., and Elmo, D., "A Combined Remote Sensing–Numerical Modelling Approach to the Stability Analysis of Delabole Slate Quarry, Cornwall, UK," *Rock Mech. Rock Eng.*, Vol. 49, No. 4, 2016, pp. 1227–1245, https://doi.org/10.1007/s00603-015-0805-z

[12] Sartori, M., Baillifard, F., Jaboyedoff, M., and Rouiller, J. D., "Kinematics of the 1991 Randa Rockslides (Valais, Switzerland)," *Nat. Hazards Earth Syst. Sci.*, Vol. 3, No. 5, 2003, pp. 423–433, https://doi.org/10.5194/nhess-3-423-2003

[13] Eberhardt, E., Stead, D., and Coggan, J. S., "Numerical Analysis of Initiation and Progressive Failure in Natural Rock Slopes—the 1991 Randa Rockslide," *Int. J. Rock Mech. Min. Sci.*, Vol. 41, No. 1, 2004, pp. 69–87, https://doi.org/10.1016/S1365-1609(03)00076-5

[14] Brideau, M. A., Yan, M., and Stead, D., "The Role of Tectonic Damage and Brittle Rock Fracture in the Development of Large Rock Slope Failures," *Geomorphology*, Vol. 103, No. 1, 2009, pp. 30–49, https://doi.org/10.1016/j.geomorph.2008.04.010

[15] Gischig, V., Loew, S., Kos, A., Moore, J. R., Raetzo, H., and Lemy, F., "Identification of Active Release Planes Using Ground-Based Differential InSAR at the Randa Rock Slope Instability, Switzerland," *Nat. Hazards Earth Syst. Sci.*, Vol. 9, No. 6, 2009, pp. 2027–2038, https://doi.org/10.5194/nhess-9-2027-2009

[16] Jiefan, H., Ganglin, C., Yonghong, Z., and Ren, W., "An Experimental Study of the Strain Field Development Prior to Failure of a Marble Plate under Compression," *Tectonophysics*, Vol. 175, Nos. 1–3, 1990, pp. 269–284, https://doi.org/10.1016/0040-1951(90)90142-U

[17] Shen, B., Stephansson, O., Einstein, H. H., and Ghahreman, B., "Coalescence of Fractures under Shear Stresses Experiments," *J. Geophys. Res.*, Vol. 100, No. B4, 1995, pp. 5975–5990, https://doi.org/10.1029/95JB00040

[18] Dyskin, A. V., Sahouryeh, E., Jewell, R. J., Joer, H., and Ustinov, K. B., "Influence of Shape and Locations of Initial 3D Cracks on Their Growth in Uniaxial Compression," *Eng. Fract. Mech.*, Vol. 70, No. 15, 2003, pp. 2115–2136, https://doi.org/10.1016/S0013-7944(02)00240-0

[19] Wong, L. N. Y. and Einstein, H. H., "Systematic Evaluation of Cracking Behavior in Specimens Containing Single Flaws under Uniaxial Compression," *Int. J. Rock Mech. Min. Sci.*, Vol. 46, No. 2, 2009, pp. 239–249, https://doi.org/10.1016/j.ijrmms.2008.03.006

[20] Zhuang, X., Chun, J., and Zhu, H., "A Comparative Study on Unfilled and Filled Crack Propagation for Rock-Like Brittle Material," *Theor. Appl. Fract. Mech.*, Vol. 72, 2014, pp. 110–120, https://doi.org/10.1016/j.tafmec.2014.04.004

[21] Lin, P., Wong, R. H. C., and Tang, C. A., "Experimental Study of Coalescence Mechanisms and Failure under Uniaxial Compression of Granite Containing Multiple Holes," *Int. J. Rock Mech. Min. Sci.*, Vol. 77, 2015, pp. 313–327, https://doi.org/10.1016/j.ijrmms.2015.04.017

[22] Zhang, X. P., Liu, Q. S., Wu, S. C., and Tang, X. H., "Crack Coalescence between Two Non-Parallel Flaws in Rock-Like Material under Uniaxial Compression," *Eng. Geol.*, Vol. 199, 2015, pp. 74–90, https://doi.org/10.1016/j.enggeo.2015.10.007

[23] Yang, S. Q., "Experimental Study on Deformation, Peak Strength and Crack Damage Behavior of Hollow Sandstone under Conventional Triaxial Compression," *Eng. Geol.*, Vol. 213, 2016, pp. 11–24, https://doi.org/10.1016/j.enggeo.2016.08.012

[24] Yang, S. Q., Huang, Y. H., Tian, W. L., and Zhu, J. B., "An Experimental Investigation on Strength, Deformation and Crack Evolution Behavior of Sandstone Containing Two Oval Flaws under Uniaxial Compression," *Eng. Geol.*, Vol. 217, 2017, pp. 35–48, https://doi.org/10.1016/j.enggeo.2016.12.004

[25] Yang, S. Q., Tian, W. L., Huang, Y. H., Ranjith, P. G., and Yu, Y., "An Experimental and Numerical Study on Cracking Behavior of Brittle Sandstone Containing Two Non-Coplanar Fissures under Uniaxial Compression," *Rock Mech. Rock Eng.*, Vol. 49, No. 4, 2016, pp. 1497–1515, https://doi.org/10.1007/s00603-015-0838-3

[26] Shah, S. P., "Fracture Toughness for High-Strength Concrete," *ACI Mater. J.*, Vol. 87, No. 3, 1990, pp. 260–265.

[27] Shah, S. P., "Experimental Methods for Determining Fracture Process Zone and Fracture Parameters," *Eng. Fract. Mech.*, Vol. 35, Nos. 1–3, 1990, pp. 3–14, https://doi.org/10.1016/0013-7944(90)90178-J

[28] Reyes, O. and Einstein, H. H., "Failure Mechanism of Fractured Rock-A Fracture Coalescence Model," presented at the *7th Congress of the ISRM*, Aachen, Germany, Sept. 16–20, 1991, International Society for Rock Mechanics and Rock Engineering, Lisbon, Portugal, pp. 333–340.

[29] Shen, B., "The Mechanics of Fracture Coalescence in Compression Experimental Study and Numerical Simulation," *Eng. Fract. Mech.*, Vol. 51, No. 1, 1995, pp. 73–85, https://doi.org/10.1016/0013-7944(94)00201-R

[30] Bobet, A., "Fracture Coalescence in Rock Materials: Experimental Observations and Numerical Predictions," Sc.D. thesis, Massachusetts Institute of Technology, Cambridge, MA, 1997.

[31] Bobet, A. and Einstein, H. H., "Fracture Coalescence in Rock-Type Materials under Uniaxial and Biaxial Compression," *Int. J. Rock Mech. Min. Sci.*, Vol. 35, No. 7, 1998, pp. 863–888, https://doi.org/10.1016/S0148-9062(98)00005-9

[32] Zhu, W. S., Chen, W. Z., and Shen, J., "Simulation Experiment and Fracture Mechanism Study on Propagation of Echelon Pattern Cracks," *Acta Mech. Solida Sin.*, Vol. 19, 2003, pp. 355–360, https://doi.org/10.1007/BF02487813

[33] Vásárhelyi, B. and Bobet, A., "Modeling of Crack Initiation, Propagation and Coalescence in Uniaxial Compression," *Rock Mech. Rock Eng.*, Vol. 33, No. 2, 2000, pp. 119–139, https://doi.org/10.1007/s006030050038

[34] Yang, S. Q. and Jing, H. W., "Strength Failure and Crack Coalescence Behavior of Brittle Sandstone Samples Containing a Single Fissure under Uniaxial Compression," *Int. J. Fract.*, Vol. 168, No. 2, 2011, pp. 227–250, https://doi.org/10.1007/s10704-010-9576-4

[35] Wong, R. H. C., Chau, K. T., Tang, C. A., and Lin, P., "Analysis of Crack Coalescence in Rock-Like Materials Containing Three Flaws—Part I: Experimental Approach," *Int. J. Rock Mech. Min. Sci.*, Vol. 38, No. 7, 2001, pp. 909–924, https://doi.org/10.1016/S1365-1609(01)00064-8

[36] Feng, X. T., Ding, W. X., and Zhang, D. X., "Multi-Crack Interaction in Limestone Subject to Stress and Flow of Chemical Solutions," *Int. J. Rock Mech. Min. Sci.*, Vol. 46, No. 1, 2009, pp. 159–171, https://doi.org/10.1016/j.ijrmms.2008.08.001

[37] Park, C. H. and Bobet, A., "Crack Coalescence in Specimens with Open and Closed Flaws: A Comparison," *Int. J. Rock Mech. Min. Sci.*, Vol. 46, No. 5, 2009, pp. 819–829, https://doi.org/10.1016/j.ijrmms.2009.02.006

[38] Park, C. H. and Bobet, A., "Crack Initiation, Propagation and Coalescence from Frictional Flaws in Uniaxial Compression," *Eng. Fract. Mech.*, Vol. 77, No. 14, 2010, pp. 2727–2748, https://doi.org/10.1016/j.engfracmech.2010.06.027

[39] Cheng, H., Zhou, X., Zhu, J., and Qian, Q., "The Effects of Crack Openings on Crack Initiation, Propagation and Coalescence Behavior in Rock-Like Materials under Uniaxial Compression," *Rock Mech. Rock Eng.*, Vol. 49, No. 9, 2016, pp. 3481–3494, https://doi.org/10.1007/s00603-016-0998-9

[40] Zhang, X. P. and Wong, L. N. Y., "Loading Rate Effects on Cracking Behavior of Flaw-Contained Specimens under Uniaxial Compression," *Int. J. Fract.*, Vol. 180, No. 1, 2013, pp. 93–110, https://doi.org/10.1007/s10704-012-9803-2

[41] Wang, Y., Zhou, X., and Xu, X., "Numerical Simulation of Propagation and Coalescence of Flaws in Rock Materials under Compressive Loads Using the Extended Non-Ordinary State-Based Peridynamics," *Eng. Fract. Mech.*, Vol. 163, 2016, pp. 248–273, https://doi.org/10.1016/j.engfracmech.2016.06.013

[42] Zhou, X. P., Bi, J., and Qian, Q. H., "Numerical Simulation of Crack Growth and Coalescence in Rock-Like Materials Containing Multiple Pre-Existing Flaws," *Rock Mech. Rock Eng.*, Vol. 48, No. 3, 2015, pp. 1097–1114, https://doi.org/10.1007/s00603-014-0627-4

[43] Haeri, H., "Propagation Mechanism of Neighboring Cracks in Rock-Like Cylindrical Specimens under Uniaxial Compression," *J. Min. Sci.*, Vol. 51, No. 3, 2015, pp. 487–496, https://doi.org/10.1134/S1062739115030096

[44] Haeri, H., "Influence of the Inclined Edge Notches on the Shear-Fracture Behavior in Edge-Notched Beam Specimens," *Comput. Concr.*, Vol. 16, No. 4, 2015, pp. 605–623, https://doi.org/10.12989/cac.2015.16.4.605

[45] Haeri, H., Shahriar, K., Marji, M. F., and Moarefvand, P., "Modeling the Propagation Mechanism of Two Random Micro Cracks in Rock Samples under Uniform Tensile Loading," presented at the *13th International Conference on Fracture*, June 16-21, 2013, Beijing, China, The Chinese Society of Theoretical and Applied Mechanics, Beijing, China, pp. 1–10.